

Electromagnon in ferrimagnetic ε -Fe₂O₃ nanograin ceramicsChristelle Kadlec,¹ Filip Kadlec,^{1,*} Veronica Goian,¹ Martí Gich,² Martin Kempa,¹ Stéphane Rols,³ Maxim Savinov,¹ Jan Prokleška,⁴ Milan Orlita,⁵ and Stanislav Kamba¹¹*Institute of Physics, Academy of Sciences of the Czech Republic, Na Slovance 2, 182 21 Prague 8, Czech Republic*²*Institut de Ciència de Materials de Barcelona—Consejo Superior de Investigaciones Científicas, Campus UAB, 08193 Bellaterra, Catalunya, Spain*³*Institut Laue-Langevin, Boîte Postale 156, 38042 Grenoble Cedex 9, France*⁴*Department of Condensed Matter Physics, Faculty of Mathematics and Physics, Charles University, Ke Karlovu 5, 121 16 Prague 2, Czech Republic*⁵*Grenoble High Magnetic Field Laboratory, CNRS-25, avenue des Martyrs, Grenoble Cedex 9, France*

(Received 26 November 2012; revised manuscript received 8 August 2013; published 4 September 2013)

Electromagnons are known from multiferroics as spin waves excited by the electric component of electromagnetic radiation. We report the discovery of an excitation in the far-infrared spectra of ε -Fe₂O₃, which we attribute to an electromagnon appearing below 110 K where the ferrimagnetic structure becomes incommensurately modulated. Inelastic neutron scattering shows that the electromagnon energy corresponds to that of a magnon from the Brillouin-zone boundary. Dielectric measurements did not reveal any sign of ferroelectricity in ε -Fe₂O₃ down to 10 K, despite its acentric crystal structure. This shows that the activation of an electromagnon requires, in addition to the polar ferrimagnetic structure, a modulation of the magnetic structure. We demonstrate that a combination of inelastic neutron scattering with infrared and/or terahertz (THz) spectroscopies allows detecting electromagnons in ceramics where no crystal-orientation analysis of THz and infrared spectra is possible.

DOI: [10.1103/PhysRevB.88.104301](https://doi.org/10.1103/PhysRevB.88.104301)

PACS number(s): 76.50.+g, 77.22.-d, 63.20.kd, 75.85.+t

I. INTRODUCTION

In past years, there has been an increasing interest in so-called multiferroic materials, displaying simultaneously spontaneous ferroelectric (FE) polarization and ferro- or antiferromagnetic (AFM) ordering. Multiferroics exhibit a rich variety of fundamental physical phenomena, and it is generally believed that they have a potential for novel applications in nonvolatile memories,^{1,2} magnonics,³ and magnetic sensors.⁴ These applications would rely on the coupling of order parameters on various time scales from quasistatic to ultrafast. However, the understanding of the microscopic mechanism of the magnetodielectric coupling is still a fundamental problem of solid-state physics. The static and dynamic magnetoelectric (ME) couplings can have different origins. Owing to the static ME coupling, the macroscopic FE polarization emerges in the cycloidal or transverse conical modulated magnetic structures; this polarization can change with the magnetic field. In contrast, the dynamic ME coupling generates an oscillatory polarization and leads to a dielectric dispersion in the terahertz (THz) region. Indeed, THz studies of multiferroics revealed a new kind of electric-field-active spin excitations contributing to the dielectric permittivity $\varepsilon = \varepsilon' - i\varepsilon''$, called electromagnons (EMs).⁵ Their characteristic feature is a coupling with polar phonons, which manifests itself in the spectra by a transfer of dielectric strength from phonons to EMs on cooling.⁶ In contrast to ferromagnetic and AFM resonances, which are magnons from the Brillouin-zone (BZ) center contributing to the magnetic permeability $\mu = \mu' - i\mu''$, the EMs can also be activated outside of the BZ center.⁷⁻¹⁰ The understanding of this fact is not trivial because the photons which excite EMs have wave vectors much smaller than the EMs. Thus, to date, there are several different theories attempting to explain the observed properties of EMs in various materials.^{7,9-11}

EMs were discovered first in TbMnO₃ and GdMnO₃,⁵ which belong to multiferroics denoted¹¹ as type II where the FE order is induced by a special magnetic ordering. Since then, EMs were confirmed in numerous type-II multiferroics.^{6,7,12-18} Other reports of EMs in type-I multiferroics [e.g., BiFeO₃ (Refs. 19–21) or hex-YMnO₃ (Ref. 22)] appear inconclusive since no transfer of the dielectric strength from polar phonons to EMs was observed.^{19,22} Also, recent infrared (IR) and THz studies did not confirm the EM in hex-YMnO₃.²³

Here, we report experiments which reveal an excitation identified as an EM in the ferrimagnetic ε phase of Fe₂O₃. Thanks to its chemical simplicity, this phase also appears as a suitable model system for theoretical studies of electromagnonic excitations. Although ε -Fe₂O₃ is quite rare and less known than the α (hematite) or γ (maghemite) phases of Fe₂O₃,²⁴ its properties make it attractive for applications, such as electromagnetic-wave absorbers and memories.²⁵⁻²⁷ Owing to limited phase stability, it can be synthesized only in the form of nanoparticles tens of nanometers in size,^{26,28} epitaxial thin films,²⁹ or nanowires a few micrometers long.³⁰ Below 480–495 K, it is ferrimagnetic;^{31,32} at room temperature, it has a collinear spin structure³³ and exhibits a coercive field of $H_c \approx 2$ T (Ref. 31)—the highest known value among metal oxides. The crystal lattice has a temperature-independent noncentrosymmetric orthorhombic structure with the $Pna2_1$ space group³⁴ (magnetic space group $Pn'a2'_1$). It consists of three crystallographically nonequivalent FeO₆ octahedra, forming chains along the a direction, and one type of FeO₄ tetrahedra.^{28,35} Compared to isostructural GaFeO₃, the low-temperature phase diagram of ε -Fe₂O₃ is complex—below 150 K, a series of magnetic phase transitions occurs. Below $T_m = 110$ K, an incommensurate magnetic ordering appears where the magnetic structure modulation has a periodicity of about ten unit cells.³⁵ Near T_m , a drop in ε' was observed,

and magnetocapacitive measurements revealed a quadratic coupling.³⁶ Room-temperature microwave measurements provided evidence of a strong ferromagnetic resonance (FMR) near 0.74 meV (frequency of 180 GHz), which can be tuned by doping with Al, Ga, or Rh.^{25–27} In order to gain insight into the dynamic ME properties of ϵ -Fe₂O₃, we obtained THz, IR, and inelastic-neutron-scattering (INS) spectra of ϵ -Fe₂O₃ nanograin ceramics upon cooling down to 10 K, providing information about polar and magnetic excitations.

II. SAMPLES AND EXPERIMENTAL METHODS

The nanoparticles of ϵ -Fe₂O₃ were synthesized by sol-gel chemistry. SiO₂-Fe₂O₃ composite gels containing 30 wt% of Fe₂O₃ were prepared from iron nitrate nonahydrate (Sigma-Aldrich > 98%) and tetraethoxysilane [(TEOS), Sigma-Aldrich 98%] in a hydroethanolic medium at a TEOS:H₂O:EtOH = 1:6:6 molar ratio. Iron nitrate was first dissolved, and then TEOS was added dropwise to the mixture under stirring. The sol was poured into 5-cm diameter Petri dishes that were closed with their covers, and gelation took place between 4 and 5 weeks. The gels were dried overnight in a stove at 70 °C, were crushed, and were thermally treated in air atmosphere for 3 h at 1100 °C (heating rate of 80 °C/h). The resulting material was a composite of ϵ -Fe₂O₃ nanoparticles of about 25 nm in diameter dispersed in an amorphous SiO₂ matrix as checked by x-ray diffraction (XRD), which did not reveal any trace of other Fe₂O₃ polymorphs. The silica was removed by stirring the composite powder for 12 h in a 12 M aqueous NaOH solution at 80 °C under reflux. XRD patterns recorded after the silica removal revealed that the microstructure and the phase stability of ϵ -Fe₂O₃ nanoparticles were not affected by the etching process. The nanoparticles were further processed by spark plasma sintering (SPS) in order to prepare a pellet suitable for dielectric, THz, and IR measurements by pressing the ϵ -Fe₂O₃ powder in a graphite mold for 4 min at 350 °C under 100 MPa. The XRD analysis of the sintered pellet showed that the SPS process did not induce any grain growth or phase transformation. Finally, the SPS pellets were polished to thin disks with a thickness of 1.2 mm. Some IR and THz measurements were performed on ϵ -Fe₂O₃ pellets with a diameter of about 6 mm, which were prepared from powder at room temperature using a standard tabletop manual hydraulic press (Perkin Elmer). The spectra were qualitatively the same, only the value of the high-frequency IR reflectance was affected by the roughness of the sample surface, which could not be polished.

IR reflectance measurements with a resolution of 0.25 meV were performed using the Fourier-transform infrared spectrometer Bruker IFS-113v in near-normal reflectance geometry with an incidence angle of 11°. An Oxford Instruments Optistat optical cryostat with polyethylene windows was used for sample cooling down to 10 K, and a liquid-He-cooled Si bolometer operating at 1.6 K was applied as a detector. We also measured far-IR reflectivity with an applied magnetic field up to 13 T. To this aim, another Bruker IFS-113v spectrometer and a custom-made superconducting magnetic cryostat allowing measurements at 2 and 4 K were used. Time-domain

THz spectroscopy was based on measurements of sample transmittance using custom-made spectrometers based on Ti:sapphire femtosecond lasers; one with an Optistat cryostat with mylar windows for measurements without a magnetic field but with a higher frequency resolution, enabling us to discern the FMR profile, and one with an Oxford Instruments Spectromag cryostat, enabling measurements with magnetic fields of up to 7 T. Here, the Voigt configuration was used with the external static magnetic field B_{ext} perpendicular to the magnetic component of the THz radiation B_{THz} . Similar effects were also observed for $B_{\text{ext}} \parallel B_{\text{THz}}$.

INS experiments were performed between 10 and 190 K using about 3 g of loose ϵ -Fe₂O₃ nanopowder in the IN4 time-of-flight diffractometer at the Institut Laue-Langevin in Grenoble, France.

III. RESULTS AND DISCUSSION

A. Broadband study of the electromagnetic response

Figure 1(a) shows the far- and mid-IR reflectivity spectra displaying polar optical phonons of ϵ -Fe₂O₃ between 10 and 300 K. Figures 1(b) and 1(c) show the far-IR $\epsilon(E)$ spectra calculated from the fits of IR reflectivity together with the experimental THz data. For this purpose, we used a model

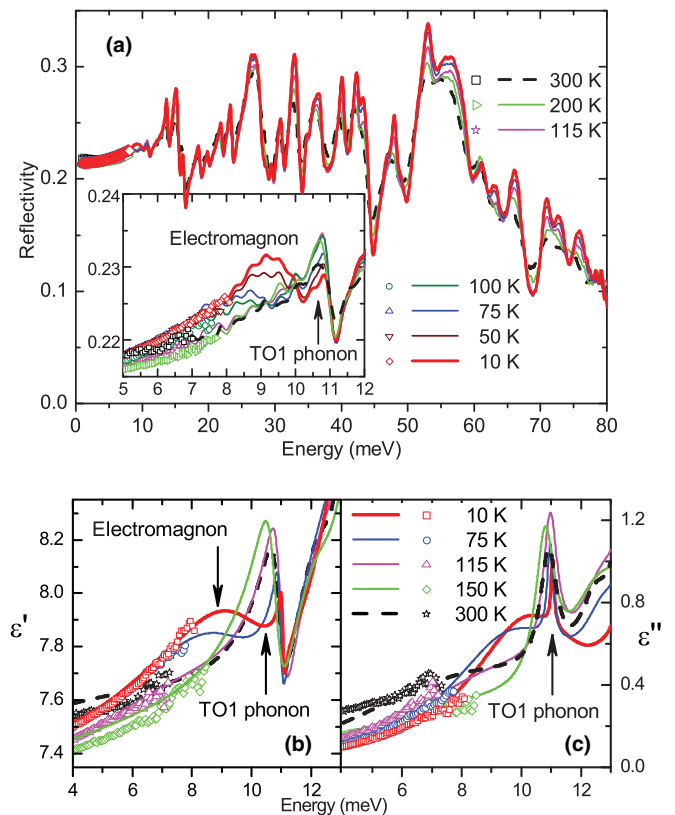


FIG. 1. (Color online) (a) Lines: IR reflectivity spectra showing polar phonons. Symbols below 8 meV: data calculated from THz spectra. The inset shows, in detail, the low-energy part where, below 100 K and 10 meV, a new reflection band appears due to the EM. (b) and (c) Fits of the complex permittivity in the far-IR region, obtained from the IR reflectivity spectra using a sum of harmonic oscillators (lines), compared to data obtained from THz spectroscopy (symbols).

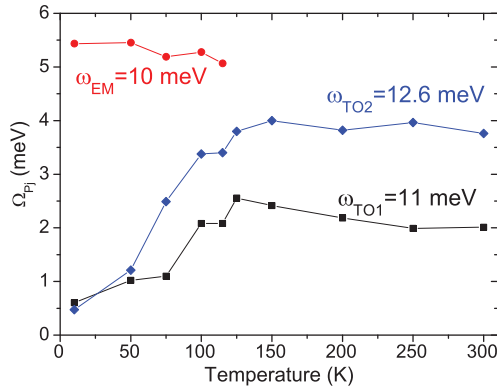


FIG. 2. (Color online) Temperature dependence of the plasma frequencies (defined as $\Omega_{pj} = \sqrt{\Delta\varepsilon_j\omega_j}$) of the 10-meV mode attributed to EM and of the TO1 and TO2 phonons. The dielectric strengths $\Delta\varepsilon_j$ were evaluated by fitting using a model with harmonic oscillators.

involving 35 harmonic oscillators; this number is lower than the number of IR active modes provided by the factor group analysis (see the Appendix); apparently, a part of the modes is too weak to be observed. Upon cooling, all phonons above 12 meV exhibit the usual behavior—their intensity increases due to reduced phonon damping at low temperatures. The TO1 phonon near 11 meV exhibits an anomalous behavior: On cooling, its intensity increases only down to 115 K. Below this temperature, it markedly weakens, whereas a supplementary broad reflectivity peak develops below $E \sim 10$ meV and becomes more intense upon cooling [see the inset of Fig. 1(a)]. This transfer of strengths also involves the TO2 phonon (see Fig. 2), evidencing a coupling among these three polar modes. Despite the lattice distortions, which occur between 150 and 75 K, the crystal symmetry of ε -Fe₂O₃ does not change with temperature.^{35,37} This is further confirmed by our IR reflectivity spectra, displaying a temperature-independent number of polar phonons; should a structural phase transition occur, it would imply a change in the factor group analysis and different phonon selection rules. Given the high number of atoms in the unit cell, multiple new reflection bands throughout the IR range would be observed. Therefore, one can exclude the new mode from originating in a structural modification.

Another option to be considered is the polar phonon splitting due to exchange coupling below AFM phase transitions, which was reported in various transition-metal monoxides and chromium spinels;³⁸ the mode splitting increased on cooling below the Néel temperature. However, this explanation cannot be valid as we observe an opposite temperature dependence—the new mode appears below T_m at low energies and hardens towards the TO1 phonon energy on cooling, i.e., their energy difference decreases.

Finally, one cannot *a priori* exclude the hypothesis of activation of the TO1 phonon branch from the area of the BZ near its edge. This would require a folding of the structural BZ, which could be caused by a transfer of the magnetic BZ folding (linked to incommensurability) via magnetostriction. Nevertheless, in the x-ray diffraction studies, no appropriate satellite reflections were observed. Even supposing these

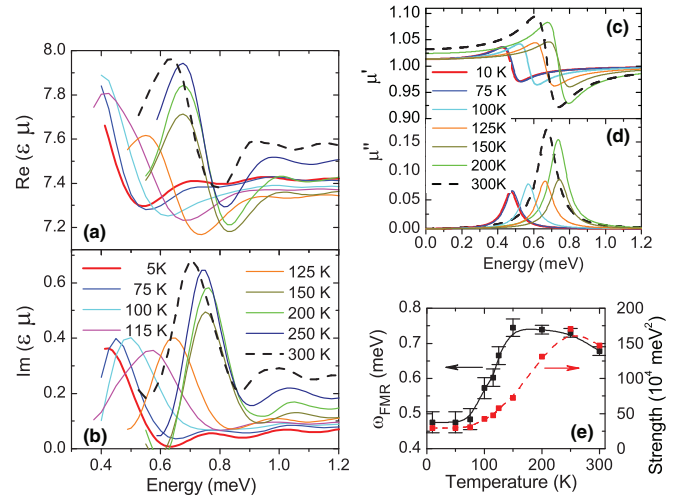


FIG. 3. (Color online) Temperature dependence of the spectra of the (a) real and (b) imaginary parts of the $\varepsilon\mu$ product, obtained by THz spectroscopy. Spectra of (c) μ' and (d) μ'' , corresponding to the FMR mode, obtained by fitting the THz spectra. (e) Temperature dependence of the FMR energy and strength $\Delta\mu\omega_{\text{FMR}}^2$ derived from parts (c) and (d).

satellite reflections to be very weak, one would expect the off-center phonons to also activate at higher energies, which we did not observe. This hypothesis, therefore, seems unlikely. Based on further experimental evidence, especially in view of an analogous temperature behavior observed by INS, below we argue that the reflection band activated below T_m is most probably an EM.

The temperature-dependent THz spectra (see Fig. 3) reveal the sharp FMR which was previously reported at room temperature.^{25,26} To quantify its temperature behavior, we used the harmonic-oscillator model for all phonons and one term accounting for the FMR in $\mu(E)$ while assuming a smooth dependence of $\varepsilon(E)$ in this interval. The resulting spectra, matching the measured data well, are shown in Figs. 3(c) and 3(d). From the fit parameters, we derived the temperature dependence of the magnon strength and FMR energy [see Fig. 3(e)]. We observe a sharp drop in the resonance energy between 150 and 75 K, very similar to that of the coercive field $H_c(T)$.³⁹ This can be explained by the fact that the FMR energy is proportional to the magnetocrystalline anisotropy field H_a . As the sample consists of randomly oriented particles with a uniaxial magnetic anisotropy, H_a is proportional to the H_c value.²⁷

Furthermore, we measured THz time-domain spectra with an external magnetic field ranging from 0 to 7 T. Because of the high absorption of the EM, lying near 10 meV, the sample was opaque above 7 meV. Therefore, we could only measure the low-frequency wing of the EM. When the magnetic field is applied, two types of changes in the THz spectra can be observed: an increase in the FMR frequency corresponding to the peak of the $\kappa(E)$ spectra and a change in the slope of both real and imaginary parts of the index of refraction, indicating shifts in the EM frequency with a magnetic field. An example of the former behavior at $T = 100$ K is shown in Figs. 4(a) and 4(b); the FMR frequency, upon applying a static magnetic

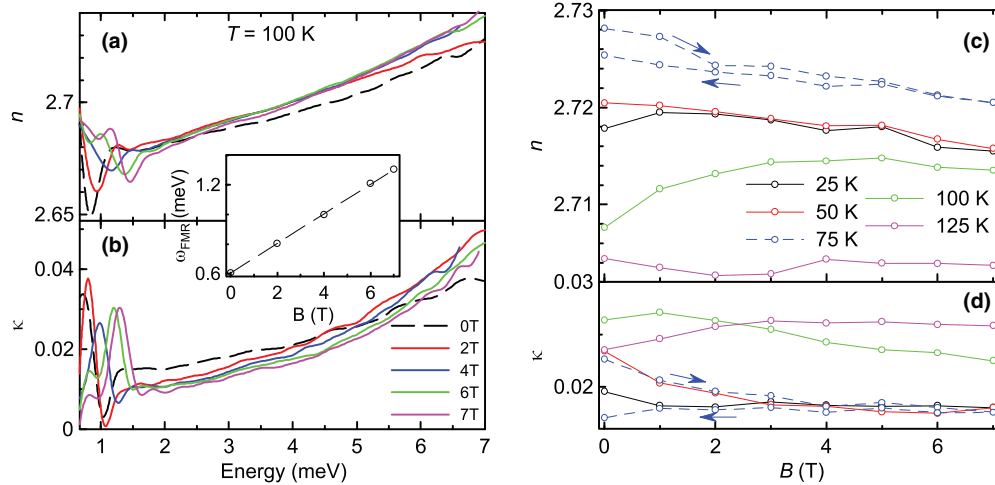


FIG. 4. (Color online) (a) and (b) Spectra of complex refractive index $N \equiv n - i\kappa$ of $\varepsilon\text{-Fe}_2\text{O}_3$ measured by THz spectroscopy at $T = 100$ K as a function of the applied magnetic field. Inset: B dependence of the FMR frequency, determined as the peak in $\kappa(E)$ spectra. (c) and (d) Changes in the value of n, κ , determined within ± 0.001 , for $E = 5$ meV as a function of temperature and increasing magnetic field (except at 75 K).

field of $B = 7$ T, increases from 0.6 to 1.3 meV [see the inset of Figs. 4(a) and 4(b)]. The latter phenomenon is illustrated by Figs. 4(c) and 4(d), which trace the values of the complex refractive index at $E = 5$ meV as a function of temperature and applied magnetic field. Although changes only close to the sensitivity level were detected at temperatures of 10 and 300 K (not shown in Fig. 4), there is a clear B dependence of the spectra at intermediate temperatures. The highest sensitivity was observed at 100 K, close to the magnetic phase transition. Also, at $T = 75$ K, a marked hysteresis in B occurs, similar to the temperature hysteresis observed by radio-frequency impedance spectroscopy techniques near this temperature (see Fig. 5); this observation will be discussed below. At $T \ll T_m$ where the magnetic structure is probably stable, the changes in N with the magnetic field are smaller. This also explains why we did not detect any significant changes in the far-IR spectra with a magnetic field at $T = 2$ K.

In the frequency range from $f = 10$ Hz to 1 MHz, the complex permittivity ε was measured by impedance spectroscopy as a function of temperature (see Fig. 6). No sign of a FE phase transition was detected. Above 200 K, both $\varepsilon'(T)$ and $\varepsilon''(T)$ increase due to the leakage conductivity and the related Maxwell-Wagner polarization. Between 100 and 200 K, we observed a steplike decrease in $\varepsilon'(T)$ towards lower temperatures and maxima in losses $\tan \delta(T, f) = \varepsilon''(T, f)/\varepsilon'(T, f)$, which is typical of a dielectric relaxation. The temperature dependence of the relaxation time $\tau(T)$, obtained from the peaks of $\tan \delta(T, f)$, follows an Arrhenius behavior, $\tau(T) = \tau_0 e^{E_0/k_B T}$ with k_B denoting the Boltzmann constant, $\tau_0 = (1.5 \pm 0.2) \times 10^{-12}$ s, and $E_0 = (0.195 \pm 0.002)$ eV. The origin of this relaxation is not clear; however, similar effects are known from several perovskite rare-earth manganites, including the multiferroics TbMnO_3 and DyMnO_3 .⁴⁰ We attribute the relaxation to thermally activated vibrations of the FE domain walls or magnetic domain walls, which can be polar.⁴¹ The huge room-temperature coercive field H_c is a consequence of a single-domain magnetic structure of the nanograins.²⁶ Below 200 K, H_c strongly decreases due

to a transition to a polydomain structure,³⁹ which explains why the dielectric relaxation exists only in this temperature range.

The inset of Fig. 6 shows the measured dependences of the polarization on an applied electric field. No open FE hysteresis loops nor signs of saturation were observed under the applied fields. Since the $Pna2_1$ crystal structure of $\varepsilon\text{-Fe}_2\text{O}_3$ corresponds to a pyroelectric space group, we cannot exclude that an applied electric field with an intensity higher than the one we used (beyond 5 kV/cm, our sample became leaky) would switch the polarization and that $\varepsilon\text{-Fe}_2\text{O}_3$ is, in fact, FE. Actually, one of us recently investigated strained epitaxial $\varepsilon\text{-Fe}_2\text{O}_3$ thin films and, under an applied electric field one order of magnitude stronger, observed a room-temperature FE switching.⁴² Since the crystal symmetry of $\varepsilon\text{-Fe}_2\text{O}_3$ does not change with temperature,⁴³ one cannot exclude that the $\varepsilon\text{-Fe}_2\text{O}_3$ nanograins are also FE already above the ferrimagnetic phase transition occurring near 490 K; in any case, it is, at least, pyroelectric. Consequently, $\varepsilon\text{-Fe}_2\text{O}_3$ would belong to type-I multiferroics.

Near 75 K, a small peak in $\varepsilon'(T)$ was observed in our impedance spectroscopy measurements (as marked by the arrow in Fig. 6). This peak is rather weak on cooling, but it becomes more distinct on heating, and it exhibits a temperature hysteresis of ≈ 15 K (see also Fig. 5). This is reminiscent of a dielectric anomaly typical for pseudoproper or improper FE phase transitions, such as those in perovskite rare-earth manganites. However, this hypothesis is not confirmed by the polarization measurements shown in Fig. 6, and the x-ray and neutron-diffraction investigations did not reveal any structural changes near 75 K.^{35,37} In type-II multiferroics, a narrow dielectric peak is seen at T_c only at frequencies below 1 MHz, and its intensity strongly decreases with rising frequency.⁴⁰ By contrast, in our impedance spectra, the peak is present at all frequencies up to the THz region [see Fig. 5(b)], although it is partly covered by the stronger dielectric relaxation at low frequencies. Therefore, this anomaly must originate from phonons or an EM. As the observed dielectric anomaly occurs

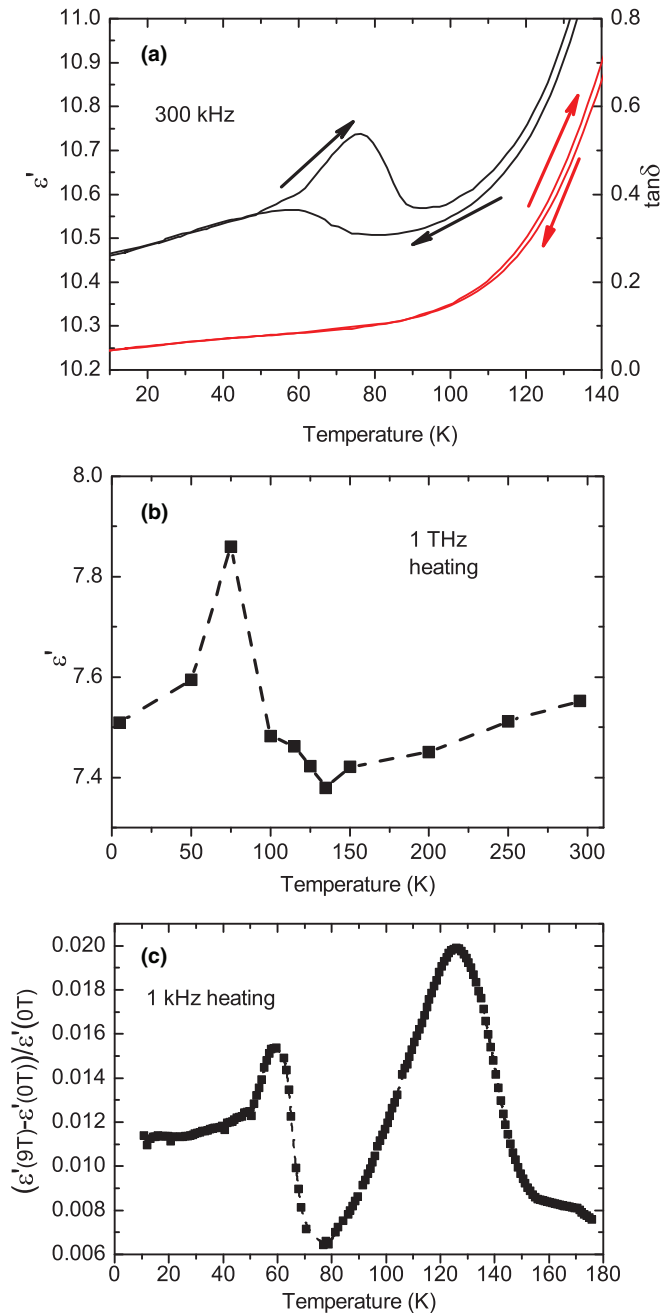


FIG. 5. (Color online) (a) Temperature hysteresis of the dielectric permittivity (black lines, left axis) and losses (red lines, right axis) observed at 300 kHz. (b) Temperature dependence of the permittivity at 1 THz measured on heating. The dashed line is a guide to the eyes. The values at 300 kHz are systematically higher than at 1 THz due to a small dielectric relaxation between these two frequencies; one can see a similar permittivity peak near 75 K in both experiments. (c) Temperature dependence of relative changes in the 1-kHz permittivity due to a magnetic field with $B = 9$ T (taken on heating).

at a temperature close to the lowest-temperature magnetic phase transition,³⁵ we propose that it arises from the transfer of the dielectric strength from the TO1 and TO2 phonons to the EM (see Fig. 2). We note that, in single-crystal multiferroics, often a steplike increase in the permittivity occurs below the temperature where the electromagnon activates.¹³ Our

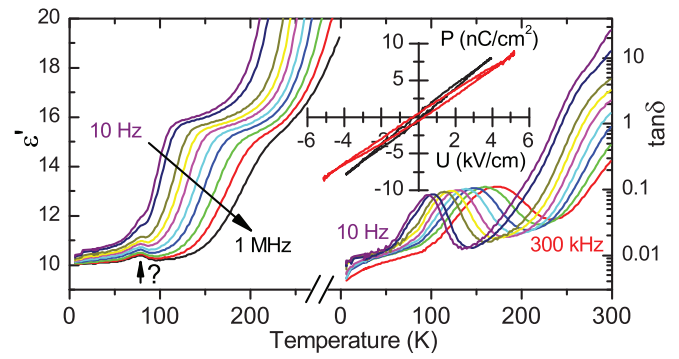


FIG. 6. (Color online) Temperature dependence of the real permittivity ε' (left) and dielectric losses $\tan\delta$ (right), measured upon heating by impedance spectroscopy. Inset: dependence of the polarization on the applied 50-Hz ac bias at 120 K (black) and 15 K (red).

observations on nanograin samples are somewhat different—whereas a steplike increase in ε' below ≈ 130 K, superimposed with the narrow-range anomaly near 75 K, was detected in the THz range [see Fig. 5(b)], only the anomaly near 75 K manifests itself in the kHz range [see Fig. 5(a)]. We suppose that the step in the low-frequency permittivity is screened by the observed dielectric relaxation in the microwave range.

We also investigated the dependence of the permittivity at 1 kHz on an external magnetic field up to 9 T. We found that $\varepsilon'(B)$ exhibits the highest changes (almost 2%) near 70 and 130 K [see Fig. 5(c)]. Both of these anomalies are clearly linked to the changes in magnetic structure.³⁵ We suppose that the lower-temperature change corresponds to the EM anomaly also observed in THz experiments, whereas that observed near 130 K is due to the relaxation linked to the magnetic and simultaneously polar domain walls.

B. Neutron scattering

In order to further explore the hypothesis of an EM, we performed time-of-flight INS experiments, which allow measuring the phonon and magnon density of states (DOS) in the meV energy range. As the nanopowder does not allow us to directly determine the phonon and magnon dispersion branches in the BZ, the data represent an orientation-averaged scattering function $S(Q, E)$, where Q is the total momentum transfer and E is the energy transferred between the crystal lattice and the neutrons (see Fig. 7). The data reveal a steep column of intense scattering, emanating from magnetic Bragg peaks at $Q = 1.4 \text{ \AA}^{-1}$ and extending up to $E \sim 10$ meV. The weaker columns at $Q > 2 \text{ \AA}^{-1}$ are due to scattering in higher-order BZs. The fact that the area of most intense scattering is located at low Q unambiguously shows⁴⁴ that the dominant contribution to the low- Q scattering comes from spin waves.

A qualitatively similar magnon response was recently observed in INS spectra of polycrystalline BiFeO_3 ,⁴⁵ the spin-wave character of the excitation was confirmed by INS on BiFeO_3 crystals where the magnon dispersion branch was directly measured.⁴⁶ Our scattering from the magnon waves becomes weaker on cooling due to the decreasing Bose-Einstein factor. Around 10 meV, a distinct scattering peak persists down to low temperatures, corresponding to a maximum of the

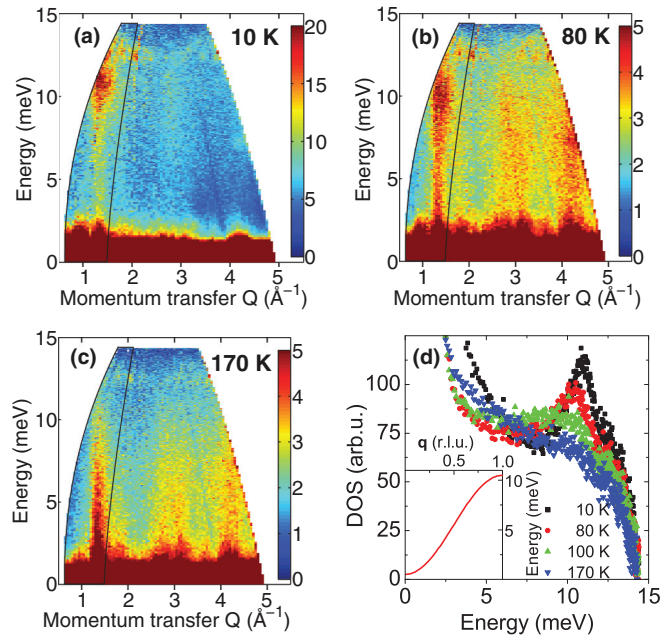


FIG. 7. (Color online) (a)–(c) Bose-Einstein-factor-normalized INS intensity as a function of momentum Q and energy E transfers for $T = 10, 80$ and 170 K. Near $Q = 1.4 \text{ \AA}^{-1}$, a magnon branch with a cutoff energy of ≈ 11 meV can be seen. (d) DOS determined by integrating over the regions marked by black solid lines in (a)–(c). Inset of (d): scheme of the magnon dispersion branch in reciprocal lattice units, involving the FMR and EM near the BZ center and boundary, respectively.

magnon DOS; this is obviously due to a flat end of the branch below the BZ boundary. Moreover, the energy at the maximal magnon DOS as well as its temperature evolution correspond to those of the newly IR-activated mode [see Fig. 7(d)].

The inset of Fig. 7(d) shows a schematic of an acousticlike magnon dispersion branch giving rise to the observed excitations, both the one below 10.5 meV (at the BZ boundary) and the FMR near 0.5 meV (in the BZ center). This dispersion behavior is similar to that observed in ferrimagnetic HoFe_2 ,⁴⁷ which exhibits a slightly higher Curie temperature of 597 K. In $\varepsilon\text{-Fe}_2\text{O}_3$, the opticlike magnon branches probably lie above 12 meV, beyond the energy range used in our INS experiments. We suggest that this acousticlike magnon is activated in the IR spectra due to the loss of magnetic translation symmetry in the incommensurate magnetic phase below T_m . Such an activation is analogous to that of phonons with $q \neq 0$ in structurally modulated crystals.⁴⁸ We suppose that the large damping of the newly activated excitation can be explained by an activation of the magnon DOS in the IR spectra. Since the observed spin-wave excitation is coupled with the lowest-energy TO1 and TO2 phonons, it must be excited by the electric component of the electromagnetic radiation; at the same time, it has to contribute to dielectric permittivity. Therefore, the excitation seen near 10 meV must be an EM.

IV. CONCLUSION

In conclusion, in $\varepsilon\text{-Fe}_2\text{O}_3$, we have discovered an excitation, appearing simultaneously with the modulation of the

magnetic structure, at energies below the TO1 phonon. We attribute this excitation to an EM whose energy corresponds to a magnon from the BZ boundary. We did not observe any other excitation at lower energies, in contrast to type-II multiferroics. There, the Dzyaloshinskii-Moriya (D.-M.) interaction breaks the center of symmetry, induces ferroelectricity,¹¹ and the EMs are activated thanks to magnetostriction [an $(\mathbf{S}_i \cdot \mathbf{S}_j)$ -type interaction].⁷ In $\varepsilon\text{-Fe}_2\text{O}_3$, the crystal structure is acentric at all temperatures, and it permits activating the D.-M. interaction in an originally collinear ferrimagnetic structure;⁴⁹ the D.-M. interaction tilts the spins and finally induces an incommensurately modulated magnetic structure below $T_m = 110$ K where the EM activates due to magnetostriction.

Up to now, EMs were reported mainly in type-II multiferroics. Previous reports of EMs in type-I multiferroics were lacking evidence of their coupling with polar phonons, e.g., in BiFeO_3 (Refs. 19–21) or hex-YMnO_3 (Ref. 22). Our results indicate that $\varepsilon\text{-Fe}_2\text{O}_3$ belongs to type-I multiferroics; it is pyroelectric and, perhaps, FE even above the ferrimagnetic phase transition⁴³ at 490 K, but the EM is activated only below T_m , corresponding to the onset of the incommensurately modulated magnetic structure. In our case, a clear transfer of dielectric strength from a low-energy phonon to the zone-boundary magnon was observed.

Finally, we would like to stress that EMs were previously identified only in single crystals using a thorough polarization analysis of measured spectra. Here, we have determined an EM from unpolarized IR and THz spectra of nanograin ceramics showing its coupling with the TO1 and TO2 phonons. Simultaneously, we have shown, from INS experiments performed on powder, that the EM in $\varepsilon\text{-Fe}_2\text{O}_3$ comes from the BZ boundary. This combination of experimental methods provides

TABLE I. Set of parameters used in the oscillator model to fit the IR reflectance data at 10 K. $\Delta\varepsilon$, Ω_0 , and Γ mark the dielectric contribution, eigenfrequency, and damping of polar modes. The first row contains the parameters of the electromagnon, and the other rows describe 35 polar phonons. From mid-IR reflectivity, the high-frequency electronic contribution was obtained as $\varepsilon_\infty = 3.2$.

| No. | $\Delta\varepsilon$ | Ω_0 (meV) | Γ (meV) | No. | $\Delta\varepsilon$ | Ω_0 (meV) | Γ (meV) |
|-----|---------------------|------------------|----------------|-----|---------------------|------------------|----------------|
| EM | 0.27 | 10.47 | 4.67 | 18 | 0.02 | 38.40 | 1.34 |
| 1 | 0.01 | 11.05 | 0.13 | 19 | 0.18 | 40.13 | 1.40 |
| 2 | 0.01 | 12.61 | 0.87 | 20 | 0.15 | 42.16 | 1.37 |
| 3 | 0.08 | 13.85 | 0.44 | 21 | 0.13 | 43.37 | 1.48 |
| 4 | 0.24 | 15.25 | 0.82 | 22 | 0.02 | 46.76 | 0.99 |
| 5 | 0.06 | 16.26 | 0.49 | 23 | 0.16 | 48.04 | 1.87 |
| 6 | 0.02 | 17.58 | 1.82 | 24 | 0.02 | 49.39 | 1.20 |
| 7 | 0.07 | 18.64 | 0.83 | 25 | 0.25 | 52.78 | 2.24 |
| 8 | 0.03 | 19.95 | 0.76 | 26 | 0.40 | 55.42 | 4.68 |
| 9 | 0.09 | 21.87 | 0.99 | 27 | 0.07 | 57.45 | 3.03 |
| 10 | 0.08 | 23.42 | 0.65 | 28 | 0.11 | 60.84 | 3.32 |
| 11 | 0.56 | 27.18 | 2.33 | 29 | 0.03 | 63.02 | 1.95 |
| 12 | 0.02 | 28.88 | 0.77 | 30 | 0.14 | 65.66 | 3.62 |
| 13 | 0.01 | 29.59 | 0.46 | 31 | 0.07 | 70.78 | 2.29 |
| 14 | 0.09 | 30.91 | 0.96 | 32 | 0.03 | 72.58 | 1.96 |
| 15 | 0.21 | 33.05 | 1.12 | 33 | 0.07 | 75.29 | 3.61 |
| 16 | 0.01 | 34.94 | 0.44 | 34 | 0.05 | 78.46 | 4.71 |
| 17 | 0.37 | 36.44 | 2.60 | 35 | 0.08 | 85.68 | 5.43 |

a guideline for an unambiguous determination of EMs in materials where sufficiently large single crystals for polarized IR and THz measurements are not available.

ACKNOWLEDGMENTS

This work was supported by the Czech Science Foundation (Project No. P204/12/1163). The experiment in ILL Grenoble was carried out at the IN4 spectrometer within the project LG11024 financed by the Ministry of Education of the Czech Republic. M.G. acknowledges funding from the Spanish Ministerio de Economía y Competitividad (Projects No. RyC-2009-04335, No. MAT 2012-35324, and No. CONSOLIDER-Nanoselect-CSD2007-00041) and the European Commission (FP7-Marie Curie Actions, Grant No. PCIG09-GA-2011-294168). S.K. thanks P. Brázda for his stimulation of our ε -Fe₂O₃ research and S. Artyukhin for a helpful discussion.

APPENDIX: PHONONS IN ε -Fe₂O₃

For the orthorhombic $Pna2_1$ crystal structure of ε -Fe₂O₃ with eight formula units per unit cell,³⁵ the factor group analysis predicts the following phonon counts and symmetries in the BZ center:

$$\Gamma = 30A_1(z, x^2, y^2, z^2) + 30A_2(xy) + 30B_1(x, xz) + 30B_2(y, yz). \quad (\text{A1})$$

Here, x , y , and z mark electric polarizations of the IR wave for which the phonons are IR active, whereas the rest of the symbols are components of the Raman tensor. After subtraction of the three acoustic phonons, 87 IR-active phonons are expected. We have observed 35 of them (see their parameters in Table I); the remaining ones cannot be identified, either because of low intensities or because they overlap with other ones.

*Corresponding author: kadlec@fzu.cz

- ¹J. Scott, *Nat. Mater.* **6**, 256 (2007).
- ²A. Roy, R. Gupta, and A. Garg, *Adv. Condens. Matter Phys.* **2012**, 926290 (2012).
- ³V. V. Kruglyak, S. O. Demokritov, and D. Grundler, *J. Phys. D: Appl. Phys.* **43**, 264001 (2010).
- ⁴C. Nan, M. Bichurin, S. Dong, D. Viehland, and G. Srinivasan, *J. Appl. Phys.* **103**, 031101 (2008).
- ⁵A. Pimenov, A. Mukhin, V. Ivanov, V. Travkin, A. Balbashov, and A. Loidl, *Nat. Phys.* **2**, 97 (2006).
- ⁶R. Valdés Aguilar, A. B. Sushkov, C. L. Zhang, Y. J. Choi, S.-W. Cheong, and H. D. Drew, *Phys. Rev. B* **76**, 060404 (2007).
- ⁷R. Valdés Aguilar, M. Mostovoy, A. B. Sushkov, C. L. Zhang, Y. J. Choi, S.-W. Cheong, and H. D. Drew, *Phys. Rev. Lett.* **102**, 047203 (2009).
- ⁸Y. Takahashi, R. Shimano, Y. Kaneko, H. Murakawa, and Y. Tokura, *Nat. Phys.* **8**, 121 (2012).
- ⁹M. P. V. Stenberg and R. de Sousa, *Phys. Rev. B* **85**, 104412 (2012); **80**, 094419 (2009).
- ¹⁰M. Mochizuki, N. Furukawa, and N. Nagaosa, *Phys. Rev. Lett.* **104**, 177206 (2010).
- ¹¹D. Khomskii, *Phys. 2*, 1 (2009).
- ¹²A. B. Sushkov, R. V. Aguilar, S. Park, S. W. Cheong, and H. D. Drew, *Phys. Rev. Lett.* **98**, 027202 (2007).
- ¹³A. B. Sushkov, M. Mostovoy, R. V. Aguilar, S.-W. Cheong, and H. D. Drew, *J. Phys.: Condens. Matter* **20**, 434210 (2008).
- ¹⁴A. Pimenov, A. M. Shuvaev, A. A. Mukhin, and A. Loidl, *J. Phys.: Condens. Matter* **20**, 434209 (2008).
- ¹⁵N. Kida, Y. Takahashi, J. Lee, R. Shimano, Y. Yamasaki, Y. Kaneko, S. Miyahara, N. Furukawa, T. Arima, and Y. Tokura, *J. Opt. Soc. Am. B* **26**, A35 (2009).
- ¹⁶S. Seki, N. Kida, S. Kumakura, R. Shimano, and Y. Tokura, *Phys. Rev. Lett.* **105**, 097207 (2010).
- ¹⁷I. Kézsmárki, N. Kida, H. Murakawa, S. Bordács, Y. Onose, and Y. Tokura, *Phys. Rev. Lett.* **106**, 057403 (2011).
- ¹⁸A. M. Shuvaev, A. A. Mukhin, and A. Pimenov, *J. Phys.: Condens. Matter* **23**, 113201 (2011).
- ¹⁹M. Cazayous, Y. Gallais, A. Sacuto, R. de Sousa, D. Lebeugle, and D. Colson, *Phys. Rev. Lett.* **101**, 037601 (2008).
- ²⁰D. Talbayev, S. A. Trugman, S. Lee, H. T. Yi, S. W. Cheong, and A. J. Taylor, *Phys. Rev. B* **83**, 094403 (2011).
- ²¹G. Komandin, V. Torgashev, A. Volkov, O. Porodinkov, I. Spektor, and A. Bush, *Phys. Solid State* **52**, 734 (2010).
- ²²S. Pailhès, X. Fabrèges, L. P. Régnault, L. Pinsard-Godart, I. Mirebeau, F. Moussa, M. Hennion, and S. Petit, *Phys. Rev. B* **79**, 134409 (2009).
- ²³C. Kadlec, V. Goian, K. Z. Rushchanskii, P. Kuzel, M. Lezaic, K. Kohn, R. V. Pisarev, and S. Kamba, *Phys. Rev. B* **84**, 174120 (2011).
- ²⁴L. Machala, J. Tuček, and R. Zbořil, *Chem. Mater.* **23**, 3255 (2011).
- ²⁵A. Namai, S. Sakurai, M. Nakajima, T. Suemoto, K. Matsumoto, M. Goto, S. Sasaki, and S. Ohkoshi, *J. Am. Chem. Soc.* **131**, 1170 (2008).
- ²⁶A. Namai, M. Yoshikiyo, K. Yamada, S. Sakurai, T. Goto, T. Yoshida, T. Miyazaki, M. Nakajima, T. Suemoto, and H. Tokoro, *Nat. Commun.* **3**, 1035 (2012).
- ²⁷S. Ohkoshi, S. Kuroki, S. Sakurai, K. Matsumoto, K. Sato, and S. Sasaki, *Angew. Chem., Int. Ed.* **46**, 8392 (2007).
- ²⁸J. Tuček, R. Zbořil, A. Namai, and S. Ohkoshi, *Chem. Mater.* **22**, 6483 (2010).
- ²⁹M. Gich, J. Gazquez, A. Roig, A. Crespi, J. Fontcuberta, J. C. Idrobo, S. J. Pennycook, M. Varela, V. Skumryev, and M. Varela, *Appl. Phys. Lett.* **96**, 112508 (2010).
- ³⁰Y. Ding, J. Morber, R. Snyder, and Z. Wang, *Adv. Funct. Mater.* **17**, 1172 (2007).
- ³¹J. Jin, S. Ohkoshi, and K. Hashimoto, *Adv. Mater.* **16**, 48 (2004).
- ³²S. Sakurai, J. Jin, K. Hashimoto, and S. Ohkoshi, *J. Phys. Soc. Japan* **74**, 1946 (2005).
- ³³J. Tuček, S. Ohkoshi, and R. Zbořil, *Appl. Phys. Lett.* **99**, 253108 (2011).
- ³⁴E. Tronc, C. Chanéac, and J. Jolivet, *J. Solid State Chem.* **139**, 93 (1998).
- ³⁵M. Gich, C. Frontera, A. Roig, E. Taboada, E. Molins, H. R. Rechenberg, J. D. Ardisson, W. A. A. Macedo, C. Ritter, V. Hardy, J. Sort, V. Skumryev, and J. Nogués, *Chem. Mater.* **18**, 3889 (2006).
- ³⁶M. Gich, C. Frontera, A. Roig, J. Fontcuberta, E. Molins, N. Bellido, C. Simon, and C. Fleta, *Nanotechnology* **17**, 687 (2006).

- ³⁷Y.-C. Tseng, N. M. Souza-Neto, D. Haskel, M. Gich, C. Frontera, A. Roig, M. van Veenendaal, and J. Nogués, *Phys. Rev. B* **79**, 094404 (2009).
- ³⁸C. Kant, M. Schmidt, Z. Wang, F. Mayr, V. Tsurkan, J. Deisenhofer, and A. Loidl, *Phys. Rev. Lett.* **108**, 177203 (2012).
- ³⁹M. Gich, A. Roig, C. Frontera, E. Molins, J. Sort, M. Popovici, G. Chouteau, D. M. y Marero, and J. Nogués, *J. Appl. Phys.* **98**, 044307 (2005).
- ⁴⁰F. Schrettle, P. Lunkenheimer, J. Hemberger, V. Y. Ivanov, A. A. Mukhin, A. M. Balbashov, and A. Loidl, *Phys. Rev. Lett.* **102**, 207208 (2009).
- ⁴¹A. Pyatakov, D. Sechin, A. Sergeev, A. Nikolaev, E. Nikolaeva, A. Logginov, and A. Zvezdin, *Europhys. Lett.* **93**, 17001 (2011).
- ⁴²M. Gich, I. Fina, A. Morelli, F. Sánchez, M. Alexe, J. Fontcuberta, and A. Roig (unpublished).
- ⁴³D. Nižňanský (private communication). (No change in the $Pna2_1$ crystal structure was observed in XRD up to 800 K.)
- ⁴⁴G. Shirane, S. M. Shapiro, and J. M. Tranquada, *Neutron Scattering with a Triple-Axis Spectrometer* (Cambridge University Press, New York, USA, 2002), pp. 36 ff.
- ⁴⁵O. Delaire, M. B. Stone, J. Ma, A. Huq, D. Gout, C. Brown, K. F. Wang, and Z. F. Ren, *Phys. Rev. B* **85**, 064405 (2012).
- ⁴⁶J. Jeong, E. A. Goremychkin, T. Guidi, K. Nakajima, G. S. Jeon, S.-A. Kim, S. Furukawa, Y. B. Kim, S. Lee, V. Kiryukhin, S.-W. Cheong, and J.-G. Park, *Phys. Rev. Lett.* **108**, 077202 (2012).
- ⁴⁷J. J. Rhyne and N. C. Koon, *J. Appl. Phys.* **49**, 2133 (1978).
- ⁴⁸J. Petzelt, *Phase Trans.* **2**, 155 (1981).
- ⁴⁹C. J. Fennie, *Phys. Rev. Lett.* **100**, 167203 (2008).